Title: FeOx nanoclusters incorporated iron phthalocyanine as highly active electrocatalysts for oxygen reduction reaction

Authors: Yi Cheng; Ji Liang; Jean-Pierre Veder; Meng Li; Shuangming Chen; Jian Pan; Li Song; Hui-Ming Cheng; Chang Liu; San Ping Jiang, Dr.

To be cited as: 10.1002/cctc.201701183

Link to VoR: https://doi.org/10.1002/cctc.201701183

FeO_x nanoclusters incorporated iron phthalocyanine as highly active electrocatalysts for oxygen reduction reaction

Yi Cheng[a], Ji Liang[b], Jean-Pierre Veder[c], Meng Li[a], Shuangming Chen[d], Jian Pan[a], Li Song[d], Hui-Ming Cheng[b], Chang Liu[b], San Ping Jiang*[,a]

[a]Fuels and Energy Technology Institute & Department of Chemical Engineering, Curtin University, Perth, WA 6102, Australia

*corresponding author: email address: S.Jiang@curtin.edu.au (SP Jiang)

[b]Shenyang National Laboratory for Materials Science, Institute of Metal Research, Chinese Academy of Sciences, Shenyang, Liaoning 110016, China.

[c]John de Laeter Centre, Curtin University, Perth, WA 6102, Australia

[d]National Synchrotron Radiation Laboratory, CAS Center for Excellence in Nanoscience, University of Science and Technology of China, 230029, Hefei, Anhui, China

Abstract:

Iron-nitrogen-carbon (Fe-N-C) composites are emerged as active and non-precious metal electrocatalysts for oxygen reduction reaction (ORR). Here, we developed a simple process to synthesize FeO_x nanoclusters (NCs) incorporated with iron phthalocyanine (FePc) supported on graphene, FeO_x/FePc, as highly active electrocatalysts for ORR via a self-assembly method. The electrochemical activity of FeO_x/FePc depends on the loading or size of FeO_x NCs. The best results are obtained on FeO_x/FePc with 10 wt% FeO_x NCs of size ~2 nm and thickness ~0.6 nm, achieving

a half-wave potential of 0.888 V and current density of 37.6 A g^{-1} at 0.9 V (vs RHE), which is 50 mV higher than FePc supported on graphene and 64 mV higher than Pt/C in 0.1 M KOH solution at a catalyst loading of 0.1 mg cm^{-2}. X-ray absorption spectroscopy and electrochemical cyclic voltammetry results indicate that incorporated FeO_x NCs interact with the active center of FePc, Fe-N_4, enhancing the electron transition and reversibility of the redox couple, Fe^{III}/Fe^{II}, and thus promoting the kinetics of the ORR. This study demonstrates evidently that nature of the active center of FePc, i.e., Fe-N_4 is closely related to the activity of Fe^{III}/Fe^{II} redox couple.

Keywords: Iron oxide nanocluster; iron phthalocyanine; Fe^{III}/Fe^{II} redox couple; active center; oxygen reduction reaction.

1 Introduction

Oxygen reduction reaction (ORR), which proceeds via a four-electron ($4e^-$) pathway to H_2O or a two-electron pathway to H_2O_2,[1, 2] plays a vital role in energy storage and conversion devices such as fuel cells and metal-air batteries.[3-6] Currently, the most-efficient ORR electrocatalysts are Pt-based materials such as Pt and $Pt_3Ni(111)$.[7, 8] However, the prohibitive cost and scarcity of Pt has simulated intensive research activities in the development of non-precious metal catalysts (NPMCs), such as heteroatom-doped carbon materials, transition metal oxides, chalcogenides and transition metal-nitrogen compounds.[9-13] Among various ORR NPMCs, iron-nitrogen-carbon, Fe-N-C based materials have been generally recognized to be the most promising alternatives for noble metal based catalysts.[4,

[14-17] A cost effective method for the facile preparation of Fe-N-C catalysts through the pyrolysis of inorganic iron salts, carbon and nitrogen precursors has been widely investigated,[4, 17-19] and significant advancements have been achieved by selection of suitable nitrogen and carbon precursors and optimization of the nanostructure.[14, 20-22]

It has been well known that iron phthalocyanine (FePc) possesses high activity for ORR and the active center, Fe-N_x plays an outstanding role in enhancing the ORR activity of the catalysts.[19, 23-31] Iron phthalocyanine that supported on carbon materials has shown an ORR performance similar to or even slightly better than the state-of-the-art Pt/C catalyst in alkaline conditions.[32-34] Iron phthalocyanine with an axial ligand anchored on single-walled carbon nanotubes, demonstrating higher electrocatalytic activity for oxygen reduction than directly supported on carbon nanotubes.[32, 35] Burkitt et al. also reported that FePc-MnO_x composite catalyst showed higher ORR current than FePc at pH7.[36] Zhang et al. recently revealed that FePc supported on manganese chloride modified graphitized carbon black could significantly improve the activity for ORR with a half wave potential positively shift by 40 mV compared that supported on graphitized carbon black. The author attributes the high performance to the Mn^{2+}-ion which can draw additional Pc groups to create more Pc-FePc complexes, which can increase the ORR catalytic activity.[37]

Here, we design an easy process by incorporating FeO_x NCs with iron phthalocyanine (FePc) supported on graphene, FeO_x/FePc, as highly active and NPMCs for ORR. The results reveal that FePc supported on graphene, FePc-G, is an

efficient ORR catalyst with activity close to Pt/C in alkaline solutions, and incorporating nano-sized FeO_x NCs significantly enhances the ORR activity of FePc.

2 Experimental

2.1 Synthesis of FeO_x NCs on FePc functionalized graphene

Purified graphene (100 mg, 1.6 nm Flakes, USA) was mixed with FePc (200 mg, FePc, Sigma-Aldrich) with a FePc:G weight ratio of 2:1 in 200 mL ethanol solution. The mixture was sonicated for 2 h, stirred for 8 h before being filtrated using a nylon membrane (0.2 μm) and washed for several times to remove the excess FePc. The as-prepared composite, denoted as FePc-G, was then dried in vacuum oven for 24 h at 71 ^{o}C.

To prepare the FeO_x NCs supported on FePc-G, the FePc-G (20 mg) was first ultrasonicated in 100 mL ethylene glycol (EG) for 1 h, followed by the addition of a certain amount of iron(III) acetylacetonate ($Fe(acac)_3$, Sigma-Aldrich). The loading or size of FeO_x NCs incorporated on FePc-G was controlled by the amount of $Fe(acac)_3$ added. For FeO_x/FePc with 10, 20 and 40 wt% FeO_x, 10.5, 23.0 and 49.0 mg $Fe(acac)_3$ were added and were denoted as FeO_x/FePc-10, FeO_x/FePc-20 and FeO_x/FePc-40, respectively. The dispersion was stirred for 1 h before it was refluxed at 100 ^{o}C for 3 h, then was filtered using a nylon filter membrane and washed for several times. Fig. 1 presents the schematic for the synthesis of FeO_x/FePc electrocatalysts. For comparison, FeO_x nanoparticles with size of around 2-3 nm supported on graphene were prepared in a similar way using polyethyleneimine (PEI, Sigma-Aldrich) functionalized graphene.[38]

2.2 Characterization

Distributions and morphology of FeO_x/FePc were studied by transmission electron microscopy (TEM) and high angle annular dark field STEM on Titan G2 60-300 at 80 kV. The atomic force microscopy (AFM) measurements were conducted on Tapping Mode using a Dimension FastScan AFM (Bruker). The catalysts were identified with X-ray diffractometer (XRD, Rigaku D/MAX RINT 2500) operated at 40 kV and 30 mA with Cu Ka (l = 1.5406 A˚) in the range of 20-90°. The loading of the FePc and FeO_x was investigated by thermogravimetric analysis (TG, Q5000). X-ray photoelectron spectroscopy (XPS) measurements were performed on a Kratos Axis Ultra DLD spectrometer using a monochromatic AlKα (1486.6 eV) irradiation source operated at 225 W. The electron binding energy scale was calibrated for each sample by setting the main line of the C 1s spectrum to 284.5 eV. XPS spectra were collected with a pass energy of 160 eV for the survey spectra and 40 eV for the high-resolution spectra. Each high-resolution spectrum was fitted with a Gaussian-Lorentzian (70%-30%) line shape with the full-width half maximum (FWHM) constrained to values considered reasonable for each element. In the case of the Fe 2p spectra in which interpretation of Fe oxidation states is known to be complicated by complex multiplet splitting, a simplified approach adapted from Lin *et. al.* was used to obtain approximate Fe^{2+}/Fe^{3+} ratios .[39] Briefly, broad peak shapes are used to quantify Fe(II) and Fe(III) components, with the shake-up satellites used as approximate guides for the positioning of the main 2p peaks. Fe K-edge X-ray absorption spectra were collected in the fluorescence mode on 1W1B beam line at the

Beijing Synchrotron Radiation Facility (BSRF) with a ring current of 250 mA at 2.5 GeV. X-ray was monochromatized by a double-crystal Si (111) monochromator. Energy calibration was carried out for each measurement by referencing a Fe metal foil standard measured at the beamline to 7112 eV and shifting all other spectra accordingly. Data reduction and processing was carried out using the Athena component of the Demeter software package.[40]

Electrochemical measurements were conducted in a standard electrochemical cell using a Princeton potentiostat (Versastat3，USA). Pt foil (3.0 cm^2) and saturated calomel electrode (SCE) with electrolytic bridge were used as the counter and reference electrodes, respectively.[41] All potentials in the present study were given versus RHE reference electrode ($E = E_{SCE} + 0.247 + 0.059pH$, here 0.247 V is the potential for SCE at 20 ^oC).

Linear scan voltammetries (LSV) were conducted to study the ORR activity at a scan rate of 10 mV s^{-1} in oxygen-saturated 0.1 M KOH solution at different rotating rates. Cyclic voltammetry was conducted at a scan rate of 50 mV s^{-1} in oxygen-saturated and nitrogen-saturated 0.1 M KOH solution without stirring. Rotating ring-disk electrode (RRDE) experiments were conducted in the same three-electrode system by using a 5.6 mm outer diameter glassy carbon disk tip and a Pt ring (inner diameter 6.25 mm, and outer diameter 7.92 mm) with collection efficiency of 26 % (Standard MT28 Series Tip, Pine Instrument Company) at a scan rate of 10 mV s^{-1} in O_2-saturated 0.1 M KOH solution with a rotating rate of 1600 rpm with catalysts loading of 0.10 mg cm^{-2}. The IR-corrected Tafel plots were recorded at

a scan rate of 1 mV s^{-1} with the electrode initially conditioned at current density of 0.5 mA cm^{-2} for 5 min.[42]

The transferred electron number per oxygen molecule involved in the oxygen reduction at electrodes was determined by the Koutechy-Levich equation given below:[43]

$$\frac{1}{j} = \frac{1}{j_k} + \frac{1}{Bw^{0.5}} \quad (1)$$

where j_k is the kinetic current and w is the electrode rotating rate. B could be determined from the slope of K-L plots based on Levich equation as follows:

$$B = 0.2nF(D_{O_2})^{2/3}v^{-1/6}C_{O_2} \quad (2)$$

where n represents the number of electrons transferred per oxygen molecule, F is the Faraday constant (F = 96485 C mol^{-1}), D_{O2} is the diffusion coefficient of O_2 in 0.1 M KOH (1.9 × 10^{-5} cm^2 s^{-1}), υ is the kinetic viscosity (0.01 cm^2 s^{-1}), and C_{O2} is the bulk concentration of O_2 (1.2 × 10^{-6} mol cm^{-3}). The constant 0.2 is adopted when the rotation speed is expressed in rpm.

3 Results and discussion

3.1 Microstructure and phase

The morphology and structure of the FePc-G and FeO_x/FePc were characterized by scanning transmission electron microscopy (STEM) and high-resolution transmission electron microscopy (HRTEM) and the results are shown in Fig.2. Typical STEM and HRTEM images reveal that FePc has been successfully assembled onto the graphene surface (Fig. 2A). In the case of FeO_x/FePc-10, STEM image

reveals that fine metal oxide NCs were homogeneously supported onto the FePc-G (Fig. 2B), and HRTEM analysis indicate that the FeO_x NCs is about 1.98±0.2 nm in dimension. FeO_x size increases as the increase of loading (Fig. 2B-C), and the average size increases to 3.02 ±0.3 nm for FeO_x/FePc-20. In the case of FeO_x/FePc-40, the average size of FeO_x is 6.48±0.4 nm. The high resolution TEM images and the fast Fourier transformed (FFT) images reveal that the FeO_x NCs are nano-crystalline, rather than amorphous (Fig.2D). And the crystalline space is in the range of 0.241, 0.228, 0.185, 0.146 and 0.134 nm which is closely related with that for Fe_3O_4 or FeOOH.[44, 45]

AFM examination indicates that FePc molecules supported on graphene is ~0.3 nm in thickness (Fig. 3A), revealing that approximately 1-2 layers of FePc has been assembled onto the graphene surface. The homogenous distribution of FePc on graphene indicates that the extended, delocalized, and conjugated π-electron system of graphene facilitates interaction with FePc through π–π stacking, producing a thin planar layer on graphene.[46, 47] The π-conjugated oligomers may assemble on graphene as a supermolecular structure driven by the moiré nanopattern of graphene.[46-48] In the case of FeO_x/FePc-10, AFM images indicate that the thickness of FeO_x NCs is ~0.6 nm (Fig. 3B), revealing that the structure is composed of 1-3 single atomic layers of octahedral coordinated metal cations typically yielding nanoplatelet morphologies. The thickness of FeO_x NCs increase as the increase of loading (Fig. 3C). In the case of FeO_x/FePc-40, the thickness of FeO_x is slightly less than 1 nm (Fig. 3C), indicating that the FeO_x NCs consist of 2-5 atomic layers.

XRD patterns of FePc-G, FeO_x/FePc-10 and FeO_x/FePc-40 (Fig. 4A) show a broad diffraction peak at 2θ of 26.12° which is corresponding to indices of (002) for graphite with a layer distance of 0.34 nm, indicating that the graphene is multilayered. The broad peak around 2θ of 60-65^o disappears with the increase of FePc loading and is most likely associated with graphene.[49] FeO_x supported on graphene is characterized with XRD peaks associated with Fe_2O_3 (PDF-330664). Nevertheless, no XRD peaks associated with Fe_2O_3 were observed on FeO_x/FePc-10 and FeO_x/FePc-40 samples. This may be related to the ultrafine and very thin FeO_x nanoclusters deposited on FePc supported on graphene, as shown that by HRTEM analysis, crystalline facets associated with Fe_2O_3 or FeOOH are clearly identified (Fig.2D). TGA curve conducted in oxygen flow shows the decomposition of the FePc-G, FeO_x/FePc-10 and FeO_x/FePc-40 (Fig. 4B), forming a reddish Fe_2O_3. The results reveal that the Fe_2O_3 amount is 6.69%, 17.72 and 42.3% for FePc, FeO_x/FePc-10 and FeO_x/FePc-40, respectively. Hence, the FePc loading was approximately 47.5% in FePc supported on graphene.

Figure 5 is the X-ray photoelectron spectroscopy (XPS) spectra of FePc-G, FeO_x/FePc and FeO_x. The N 1s curves (Fig. 5A) clearly show two peaks around 398.8 and 399.5 eV for FePc, corresponding to two distinct nitrogen bonding environments relating to pyridine-like nitrogen (i.e. nitrogen atoms with two carbon neighbors in an aromatic ring) and Fe-N_x, respectively.[20] These two peaks are slightly positively shifted to 398.8 and 400.1 eV for FeO_x/FePc-10 and 398.8 and 400.2 eV for FeO_x/FePc-40, implying a change in the local bonding environment of nitrogen in the

FePc with the incorporation of FeO_x NCs. The measured Fe:N ratio of the FePc-G sample is 1:7.6, close to the ideal Fe:N ratio of 1:8. The contents for FePc in FeO_x/FePc-10 and FeO_x/FePc-40 were determined to be 13.4 % and 11.7 %, respectively. The low contribution of FePc to the XPS signal in FeO_x/FePc-10 and FeO_x/FePc-40 is consistent with the STEM, HRTEM and AFM results, suggesting that the FeO_x forms a thin layer of NCs over the FePc which suppresses the contribution to the XPS signal from FePc because XPS is a surface-sensitive technique.

Figure 5B presents the Fe 2p spectra of FeO_x, FePc-G, FeO_x/FePc-10 and FeO_x/FePc-40. The binding energy (BE) for Fe $2p_{2/3}$ and Fe $2p_{1/2}$ is 711.2 and 724.8 eV for FeO_x/FePc-10, approximately 0.8 and 0.7 eV higher than that for FePc-G, and 0.2 and 0.1 eV lower than BE of 711.4 and 724.9 eV for FeO_x, respectively. The positive shift and the negative shift of Fe 2p of FeO_x/FePc-10 as compared to that in FePc and in FeO_x NCs, respectively, indicating the donation of electron from FePc to FeO_x NCs. In the deconvoluted spectra, it is apparent that each sample contains a mixture of Fe(II) and Fe(III) species. The Fe(II):Fe(III) ratios gradually decrease with increasing FeO_x:FePc ratio. Fe(II):Fe(III) ratios were determined to be 1:1.1, 1:2.4, 1:2.5 and 1:3.2 for FePc-G, FeO_x/FePc-10, FeO_x/FePc-40 and FeO_x, respectively. The presence of Fe(III) in FePc is attributed to a compound effect of partial oxidation of FePc and the covalent bonding of the FePc to oxygen containing functional groups, e.g. carboxyl on graphene surface. In the case of the FeO_x sample, the dominant contribution of Fe(III) to the Fe 2p spectrum of FeO_x suggests that FeO_x is mainly

comprised of Fe_2O_3 or FeOOH.

The O 1s spectra of samples further explains the identity of the FeO_x NCs and the nature of the interaction with FePc and the graphene support. Deconvolution of the O 1s spectrum of FePc-G (Fig. 5C) yields four peaks, namely: (i) Fe-O: 529.9 eV, (ii) Fe-O-C bonds linking FePc to G (531.3 eV), (iii) oxygen in carboxylate and/or carbonyl (O-C=O; C=O: 532.2 eV), and (iv) the oxygen in epoxy and/or hydroxyl (C-O-C; C-OH: 533.3 eV).[50] The presence of Fe-O and Fe-O-C suggests the presence of Fe(III) in the sample because FePc is partially oxidized and also covalently bonded to the graphene support. Addition of FeO_x also likely results in the emergence of a new peak associated with lattice hydroxides (e.g. FeOOH) that directly overlaps the peak associated with Fe-O-C.[51] The emergence of such a peak, in addition to the findings from the Fe 2p spectra, confirms that FeOOH is the predominant phase of FeO_x. Table 1 summarizes the relative concentration of typical species and the peak position from XPS.

The structures of FePc-G, FeO_x/FePc-10, FeO_x/FePc-40 and FeO_x were also characterized by X-ray absorption spectroscopy (X-ray absorption near edge structures, XANES, and X-ray absorption fine structure, XAFS). Figure 6A shows the XANES spectra of FePc-G, FeO_x/FePc and FeO_x. A strong pre-edge peak at 7114.1 eV is observed in all samples, which is associated with unfilled d-orbitals of transition metals and is assigned to the 1s to 3d transition.[52] The FePc-G exhibits a relatively strong pre-edge peak which suggests that FePc is largely oxidized probably due to the covalently bonding of the FePc with the carboxyl groups on graphene.[53] Evidence of

the existence of pure FePc in FePc-G and FeO_x/FePc can be drawn from the first differential XANES spectra (Fig. 6A) in which a shoulder is clearly evident at 7118.3 eV, corresponding to a dipole-allowed 1s → 4p transition. Similar observations were noted by Kim, *et al.* for FePc adsorbed onto carbon powder.[53] The results reveal that (i) some FePc molecules may be distorted upon adsorption so that D_{4h} symmetry is no longer maintained, or (ii) part of the FePc was oxidized resulting in symmetry breaking from D_{4h} for FePc to C_{4v} for $(FePc)_2O$ when the μ-oxo structure is formed.[53, 54] This finding is consistent with the Fe 2p and O 1s XPS spectra which support the existence of an oxidized form of FePc that covalently bonded to carboxyl groups on graphene.

The XANES and EXAFS spectra (Fig. 6B) for the FePc-G sample closely resemble the spectra of $(FePc)_2O$ obtained by Kim *et al.*[54] The first peak in the Fourier Transform Fe K-edge spectrum for the FePc sample (labelled peak I) arises due to the Fe-O interaction characteristic of $(FePc)_2O$. The second major peak (peak II) at *ca.* 1.65 Å (before phase shift correction) is due to backscattering from the four N_p atoms surrounding the central Fe atom.[53] In the case of the FeO_x sample, peak III at 1.45 Å corresponds to lattice Fe-O scattering in the FeO_x structure, while peak IV at 2.80 Å corresponds to Fe-Fe scattering.[30, 55] FeO_x/FePc-10 and FeO_x/FePc-40 possess shared traits to that of the FePc and the FeO_x FT spectra, with the major peak at *ca.* 1.55 Å, representing a mixture of Fe-O/N scattering paths. The spectra corresponding to the FeO_x/FePc-10 sample shows a broad peak with a shoulder around 1-2 Å, revealing the strong interaction of the Fe-N_x with the Fe-O bonding

environment of the adjacent FeO_x NCs.

3.2 Oxygen reduction reaction activity

ORR activities of FeO_x/FePc, FePc-G and FeO_x were investigated in O_2-saturated 0.1 KOH solutions. FeO_x shows a very low activity for ORR with an onset potential of 0.880 V and a half-wave potential of 0.625 V (Fig. 7A). FePc-G shows a much better activity for ORR with an onset potential of 0.960 V and half-wave potential of 0.838 V, revealing that Fe-N_4 is very active and acts as the major active center for ORR, consistent with the reported results.[22, 56] FeO_x/FePc-10 exhibits significantly improved ORR activity with an onset potential of 0.99 V and a half-wave potential of 0.888 V, which is 30 mV and 50 mV higher than that of FePc-G. The half-wave potential of FeO_x/FePc-10 is even 62 mV higher than that of Pt/C under identical catalyst loading of 0.1 mg cm^2. The current density for FeO_x/FePc-10 is 1.92 mA cm^{-2} (i.e., 37.6 A g^{-1}) at 0.9 V, which is about 3.1 times of 0.62 mA cm^{-2} (i.e., 12.1 A g^{-1}) measured on Pt/C, and ~3.0 times of 0.65 mA cm^{-2} (i.e., 12.7 A g^{-1}) measured on FePc-G (Fig. 7B). To the best of our knowledge, the half-wave potential value of 0.888 V is among the highest in NPMCs reported to date (see Table 2).[21, 33, 57-65] For example, Chen et al developed an atomically dispersed Fe-N-C and showed an onset potential of 0.95 V and half-wave potential of 0.85 V with catalyst loading of 0.6 mg cm^{-2}.[21] Ma et al. synthesized a N and P co-doped carbon materials exhibiting a half wave potential of 0.87 V.[59] The present study demonstrates that the fine FeO_x NCs incorporated FePc supported on graphene is very active for ORR. The ORR activity slightly decreases as the FeO_x loading or size increases. As the FeO_x loading

increased to 40wt%, FeO_x/FePc-40, the geometric and mass specific current density at 0.9 V decreased slightly to 1.31 mA cm^{-2} and 25.6 A g^{-1}, respectively. The onset potential and half-wave potential of FeO_x/FePc-40 were 0.96 V and 0.862 V, respectively, which is 30 and 26 mV lower than that of FeO_x/FePc-10.

The improved ORR activity of the FeO_x/FePc catalysts is also supported by rotating ring-disk electrode studies that shows substantially smaller ring current densities (j_R), indicative of a lower H_2O_2 yield during the ORR process (Fig. 7C). The j_R for FePc-G increased from 0.02 mA/cm^{-2} to 0.05 mA/cm^{-2} as the potential decreased from 0.8 to 0.2 V, which is similar with that for ORR on Pt/C but significantly lower than that on FeO_x. On the other hand, the FeO_x/FePc-10 shows remarkable efficiency with the j_R close to zero in the potential range of 1.0-0.2 V. The H_2O_2 yield and the electron transfer number are calculated according to the following formulas:[66]

$$H_2O_2\% = \frac{200\frac{I_R}{N}}{(\frac{I_R}{N} + I_D)} \quad (1)$$

$$n = \frac{4I_D}{(\frac{I_R}{N} + I_D)} \quad (2)$$

where I_D is the disk current, I_R is the ring current, N is the collection efficiency and n is the electron transfer number. The H_2O_2 yield is ~2% for Pt/C and 2-4% for FePc-G. In the case of FeO_x/FePc-10, the H_2O_2 yield is less than 1% (Fig. 7D). The electron transfer number for FeO_x/FePc-10 is *ca.* 3.99 in the potential range of 0.2-0.1 V, slightly higher than that of 3.95 for FePc-G and Pt/C, revealing that the ORR on FeO_x/FePc proceeds through a 4-electron transfer process with negligible H_2O_2 yield.

The ORR mechanism was further investigated at different stirring rates (Fig. 8A-D). The kinetic currents are extracted from the measured currents at 0.8 V using Koutecký-Levich (K-L) equation. The K-L plots measured at 0.8 V (Fig. 8E) shows a similar slope for the reaction on FeO_x/FePc and Pt/C. The electron transfer number was calculated to be 3.85, 4.03, 3.96, 3.91 for the reaction on FePc-G, FeO_x/FePc-10, FeO_x/FePc-40 and Pt/C, respectively, again confirming that the ORR on FeO_x/FePc precedes through a four-electron process. The Tafel slope was 32 mV/dec for FePc-G and 29 mV dec^{-1} for FeO_x/FePc-10, which is significantly lower than 70 mV for the reaction on Pt/C (Fig. 8F). This is also lower than 40 mV/dec reported for the most active Pt-Ni alloy.[67] Similar Tafel slopes for the reaction on FePc-G and FeO_x/FePc-10 further reveal that the Fe-N_x is the major active center for ORR.

3.3 Promotion effect of incorporated FeO_x in FePc

Figure 9 is the cyclic voltammograms (CVs) conducted under N_2-saturated and O_2 saturated 0.1 M KOH solutions for FeO_x, FePc-G, FeO_x/FePc-10 and FeO_x/FePc-40. FePc-G shows a high redox activity with three reversible redox peaks at 1.428-1.450 V, 0.826-0.840 V, 0.290-0.310 V (Fig. 9A), which can be assigned to the transition of Fe^{IV}/Fe^{III}, Fe^{III}/Fe^{II} and Fe^{II}/Fe^{I} redox couples.[68, 69] The separation potential of the cathodic and anodic peak, ΔE_p, is ~20 mV for Fe^{III}/Fe^{II} redox couples on FePc-G. By comparison, FeO_x shows a very low redox activity and cathodic and anodic peaks for the redox couples are negligible. Incorporation of FeO_x NCs significantly changes the electrochemical behavior of the redox couples of FePc, particularly for Fe^{III}/Fe^{II}. The reduction potential for Fe^{III}/Fe^{II} of FeO_x/FePc-10 is

0.863 V, anodically shifted by 42 mV, as compared with that of FePc-G. The ΔE_p for the Fe^{III}/Fe^{II} redox couple of FeO_x/FePc-10 is 0 mV, significantly smaller than 20 mV for the same redox couple of FePc-G. In the case of FeO_x/FePc-40 catalysts, ΔE_p for Fe^{III}/Fe^{II} redox couple is also 0 mV, but the reduction potential was negatively shift by 12 mV, smaller than that of FeO_x/FePc-10. This is consistent with the slightly decreased activity of FeO_x/FePc-40. The substantially reduced ΔE_p indicates that the Fe^{III}/Fe^{II} redox reaction is much faster and more reversible on FeO_x/FePc than that on FePc-G. The CV curves obtained in the O_2-saturated 0.1 M KOH solution reveal that the three redox couples for Fe^{IV}/Fe^{III}, Fe^{III}/Fe^{II} and Fe^{II}/Fe^{I} are still visible. However, the reduction peak for Fe^{III}/Fe^{II} was positively shifted by 25 mV and their intensity significantly increased due to the increase of electron transfer during ORR. These results indicate that in both FePc-G and FeO_x/FePc catalysts, the active center would be the same. This implies that the nature of active center, i.e, Fe-N_4 is closely related to Fe^{III}/Fe^{II} redox couple, which provides the electron transfer for ORR. Incorporation of FeO_x NCs accelerates the electron transfer and promotes reversibility of Fe^{III}/Fe^{II} redox couple, thus enhancing the ORR activity of FePc, as shown in this study.

Li et al. investigated the structural and mechanistic basis for the high activity of FeN_xC_y catalysts for ORR.[30] The close correlation between the Fe^{III}/Fe^{II} redox potential and the onset of ORR has been rationalized by the findings that the number of available active sites decreases sharply with the applied potential crossing the redox potential anodically. This indicated that the Fe^{III}/Fe^{II} redox potential plays a dominant role for the catalytic activity of FeN_xC_y. Combined *ex situ* and *in*

situ characterizations also identified a non-planar ferrous Fe–N_4 moiety embedded in distorted carbon matrix characterized by a Fe^{III}/Fe^{II} redox couple as the active site for ORR.[30] The fast redox reaction of Fe^{III}/Fe^{II} on FeO_x/FePc is most likely due to a down shift in energy level of e_g-orbitals of the iron center away from the Fermi level as shown by the XPS results, hence leading to higher ORR onset potential and optimized adsorption strength of ORR intermediates.[70, 71] Figure 10 presents the schematic of promotion effect of incorporated FeO_x on the ORR on FeO_x/FePc.

4 Conclusions

In this study, we have demonstrated that incorporating the ultrafine FeO_x NCs with FePc can significantly improve the ORR activity of FePc based electrocatalysts. The results that the nature of the active center, Fe-N_4 of FePc is closely related to the Fe^{III}/Fe^{II} redox couple and the incorporated FeO_x NCs promote the electron transfer and reversibility of the Fe^{III}/Fe^{II} redox couple, leading the significant improvement of the activity for ORR. Such promotion effect is most likely due to the withdrawal of electrons from FePc and a down shift in energy level of e_g-orbitals of the iron center away from the Fermi level. The size of the FeO_x NCs (in the range of 2-5 nm with thickness of around 1 nm) plays a minor role in tuning the ORR activity under the conditions of the present study. FeO_x/FePc-G-10 with FeO_x nanoclusters of size ~2 nm and thickness less than 0.6 nm have been demonstrated to be one of the best non-noble metal oxygen catalysts, achieving an onset potential of 0.99 V and half-wave potential of 0.888 V which is better than Pt/C catalysts. This study provides a new and facile strategy to develop high-performance electrocatalysts for ORR in

alkaline solutions.

Acknowledgment

This research was supported by the Australian Research Council Discovery Project Funding Scheme (project number: DP150102044 and DP150102025). The authors acknowledge the facilities, and the scientific and technical assistance of Assoc/Prof Martin Saunders of the National Imaging Facility at the Centre for Microscopy, Characterization & Analysis, the University of Western Australia, a facility funded by the University, State and Commonwealth Governments, as well as the WA X-ray Surface Analysis Facility, funded by the Australian Research Council LIEF grant LE120100026. We thank the Beijing Synchrotron Radiation Facility (1W1B, BSRF) for characterizations.

References:

[1] N. Ramaswamy, S. Mukerjee *Advances in Physical Chemistry*. **2012**, 2012, 17.
[2] I. Katsounaros, W. B. Schneider, J. C. Meier, U. Benedikt, P. U. Biedermann, A. A. Auer, K. J. J. Mayrhofer *Physical Chemistry Chemical Physics*. **2012**, 14, 7384-7391.
[3] M. K. Debe *Nature*. **2012**, 486, 43-51.
[4] M. Lefèvre, E. Proietti, F. Jaouen, J.-P. Dodelet *Science*. **2009**, 324, 71-74.
[5] Z. L. Wang, D. Xu, J. J. Xu, X. B. Zhang *Chemical Society Reviews*. **2014**, 43, 7746-7786.
[6] H. B. Yang, J. Miao, S.-F. Hung, J. Chen, H. B. Tao, X. Wang, L. Zhang, R. Chen, J. Gao, H. M. Chen, L. Dai, B. Liu *Science Advances*. **2016**, 2.
[7] T. Reier, M. Oezaslan, P. Strasser *Acs Catalysis*. **2012**, 2, 1765-1772.
[8] V. R. Stamenkovic, B. Fowler, B. S. Mun, G. Wang, P. N. Ross, C. A. Lucas, N. M. Markovic *Science*. **2007**, 315, 493-497.
[9] M. Shao, Q. Chang, J.-P. Dodelet, R. Chenitz *Chemical Reviews*. **2016**, 116, 3594-3657.
[10] D. Chen, C. Chen, Z. M. Baiyee, Z. Shao, F. Ciucci *Chemical Reviews*. **2015**, 115, 9869-9921.
[11] X. Huang, L.-J. Zhou, D. Voiry, M. Chhowalla, X. Zou, T. Asefa *ACS Applied Materials & Interfaces*. **2016**, 8, 18891-18903.
[12] X. Huang, X. Zou, Y. Meng, E. Mikmeková, H. Chen, D. Voiry, A. Goswami, M. Chhowalla, T. Asefa *ACS Applied Materials & Interfaces*. **2015**, 7, 1978-1986.
[13] Y. Meng, D. Voiry, A. Goswami, X. Zou, X. Huang, M. Chhowalla, Z. Liu, T. Asefa *Journal of the*

American Chemical Society. **2014**, 136, 13554-13557.
[14] G. Wu, K. L. More, C. M. Johnston, P. Zelenay *Science*. **2011**, 332, 443-447.
[15] Y. Zhao, K. Watanabe, K. Hashimoto *Journal of the American Chemical Society*. **2012**, 134, 19528-19531.
[16] L. Lin, Q. Zhu, A.-W. Xu *Journal of the American Chemical Society*. **2014**, 136, 11027-11033.
[17] J. Tian, A. Morozan, M. T. Sougrati, M. Lefèvre, R. Chenitz, J.-P. Dodelet, D. Jones, F. Jaouen *Angewandte Chemie International Edition*. **2013**, 52, 6867-6870.
[18] J. Liang, R. F. Zhou, X. M. Chen, Y. H. Tang, S. Z. Qiao *Advanced Materials*. **2014**, 26, 6074-6079.
[19] A. Zitolo, V. Goellner, V. Armel, M.-T. Sougrati, T. Mineva, L. Stievano, E. Fonda, F. Jaouen *Nat Mater*. **2015**, 14, 937-942.
[20] W.-J. Jiang, L. Gu, L. Li, Y. Zhang, X. Zhang, L.-J. Zhang, J.-Q. Wang, J.-S. Hu, Z. Wei, L.-J. Wan *Journal of the American Chemical Society*. **2016**, 138, 3570-3578.
[21] P. Chen, T. Zhou, L. Xing, K. Xu, Y. Tong, H. Xie, L. Zhang, W. Yan, W. Chu, C. Wu, Y. Xie *Angewandte Chemie International Edition*. **2017**, 56, 610-614.
[22] Y. J. Sa, D.-J. Seo, J. Woo, J. T. Lim, J. Y. Cheon, S. Y. Yang, J. M. Lee, D. Kang, T. J. Shin, H. S. Shin, H. Y. Jeong, C. S. Kim, M. G. Kim, T.-Y. Kim, S. H. Joo *Journal of the American Chemical Society*. **2016**, 138, 15046-15056.
[23] X. Chen, F. Li, N. Zhang, L. An, D. Xia *Physical Chemistry Chemical Physics*. **2013**, 15, 19330-19336.
[24] A. H. A. Monteverde Videla, S. Ban, S. Specchia, L. Zhang, J. Zhang *Carbon*. **2014**, 76, 386-400.
[25] S. Kattel, P. Atanassov, B. Kiefer *Physical Chemistry Chemical Physics*. **2014**, 16, 13800-13806.
[26] E. F. Holby, G. Wu, P. Zelenay, C. D. Taylor *The Journal of Physical Chemistry C*. **2014**, 118, 14388-14393.
[27] M. S. Thorum, J. M. Hankett, A. A. Gewirth *The Journal of Physical Chemistry Letters*. **2011**, 2, 295-298.
[28] S. Ganesan, N. Leonard, S. C. Barton *Physical Chemistry Chemical Physics*. **2014**, 16, 4576-4585.
[29] Y. Zhu, B. Zhang, D.-W. Wang, D. S. Su *ChemSusChem*. **2015**, 8, 4016-4021.
[30] J. Li, S. Ghoshal, W. Liang, M.-T. Sougrati, F. Jaouen, B. Halevi, S. McKinney, G. McCool, C. Ma, X. Yuan, Z.-F. Ma, S. Mukerjee, Q. Jia *Energy & Environmental Science*. **2016**, 9, 2418-2432.
[31] Q. Jia, N. Ramaswamy, H. Hafiz, U. Tylus, K. Strickland, G. Wu, B. Barbiellini, A. Bansil, E. F. Holby, P. Zelenay, S. Mukerjee *ACS Nano*. **2015**, 9, 12496-12505.
[32] R. Cao, R. Thapa, H. Kim, X. Xu, M. Gyu Kim, Q. Li, N. Park, M. Liu, J. Cho *Nature Communications*. **2013**, 4, 2076.
[33] T. Taniguchi, H. Tateishi, S. Miyamoto, K. Hatakeyama, C. Ogata, A. Funatsu, S. Hayami, Y. Makinose, N. Matsushita, M. Koinuma, Y. Matsumoto *Particle & Particle Systems Characterization*. **2013**, 30, 1063-1070.
[34] Z. Zhang, X. Gao, M. Dou, J. Ji, F. Wang *Journal of Materials Chemistry A*. **2017**, 5, 1526-1532.
[35] M. Li, X. Bo, Y. Zhang, C. Han, L. Guo *Journal of Power Sources*. **2014**, 264, 114-122.
[36] R. Burkitt, T. R. Whiffen, E. H. Yu *Applied Catalysis B: Environmental*. **2016**, 181, 279-288.
[37] Z. Zhang, M. Dou, J. Ji, F. Wang *Nano Energy*. **2017**, 34, 338-343.
[38] Y. Cheng, J. Pan, M. Saunders, S. Yao, P. K. Shen, H. Wang, S. P. Jiang *RSC Advances*. **2016**, 6, 51356-51366.
[39] T.-C. Lin, G. Seshadri, J. A. Kelber *Applied Surface Science*. **1997**, 119, 83-92.

[40] B. Ravel, M. Newville *Journal of Synchrotron Radiation*. **2005**, 12, 537-541.
[41] Y. Cheng, S. P. Jiang *Electrochimica Acta*. **2013**, 99, 124-132.
[42] D. K. Bediako, Y. Surendranath, D. G. Nocera *Journal of the American Chemical Society*. **2013**, 135, 3662-3674.
[43] S. Wang, D. Yu, L. Dai *Journal of the American Chemical Society*. **2011**, 133, 5182-5185.
[44] T. Nagai, H. Kagi, T. Yamanaka *American Mineralogist*. **2003**, 88, 1423-1427.
[45] A. F. Gualtieri, P. Venturelli *American Mineralogist*. **1999**, 84, 895-904.
[46] H. Y. Mao, R. Wang, Y. Wang, T. C. Niu, J. Q. Zhong, M. Y. Huang, D. C. Qi, K. P. Loh, A. T. S. Wee, W. Chen *Applied Physics Letters*. **2011**, 99.
[47] M. Scardamaglia, G. Forte, S. Lizzit, A. Baraldi, P. Lacovig, R. Larciprete, C. Mariani, M. G. Betti *Journal of Nanoparticle Research*. **2011**, 13, 6013-6020.
[48] J. Mao, H. Zhang, Y. Jiang, Y. Pan, M. Gao, W. Xiao, H. J. Gao *Journal of the American Chemical Society*. **2009**, 131, 14136-14137.
[49] Y. Cheng, S. Dou, J. P. Veder, S. Wang, M. Saunders, S. P. Jiang *Acs Applied Materials & Interfaces*. **2017**, 9, 8121-8133.
[50] N. A. Zubir, C. Yacou, J. Motuzas, X. Zhang, J. C. Diniz da Costa *Scientific Reports*. **2014**, 4, 4594.
[51] A. P. Grosvenor, B. A. Kobe, N. S. McIntyre *Surface Science*. **2004**, 572, 217-227.
[52] C. Piquer, M. A. Laguna-Marco, A. G. Roca, R. Boada, C. Guglieri, J. Chaboy *The Journal of Physical Chemistry C*. **2014**, 118, 1332-1346.
[53] S. Kim, T. Ohta, G. Kwag *Bulletin of the Korean Chemical Society*. **2000**, 21, 588-594.
[54] H. J. Choi, G. Kwag, S. Kim *Journal of Electroanalytical Chemistry*. **2001**, 508, 105-114.
[55] B. Koo, H. Xiong, M. D. Slater, V. B. Prakapenka, M. Balasubramanian, P. Podsiadlo, C. S. Johnson, T. Rajh, E. V. Shevchenko *Nano Letters*. **2012**, 12, 2429-2435.
[56] J.-Y. Gu, Z.-F. Cai, D. Wang, L.-J. Wan *ACS Nano*. **2016**, 10, 8746-8750.
[57] J.-S. Li, S.-L. Li, Y.-J. Tang, M. Han, Z.-H. Dai, J.-C. Bao, Y.-Q. Lan *Chem. Commun.* **2015**, 51, 2710-2713.
[58] P.-J. Wei, G.-Q. Yu, Y. Naruta, J.-G. Liu *Angewandte Chemie International Edition*. **2014**, 53, 6659-6663.
[59] R. Li, Z. Wei, X. Gou *Acs Catalysis*. **2015**, 5, 4133-4142.
[60] R. Cao, R. Thapa, H. Kim, X. Xu, M. Gyu Kim, Q. Li, N. Park, M. Liu, J. Cho *Nat Commun*. **2013**, 4.
[61] Y. Su, Y. Zhu, H. Jiang, J. Shen, X. Yang, W. Zou, J. Chen, C. Li *Nanoscale*. **2014**, 6, 15080-15089.
[62] G.-L. Tian, M.-Q. Zhao, D. Yu, X.-Y. Kong, J.-Q. Huang, Q. Zhang, F. Wei *Small*. **2014**, 10, 2251-2259.
[63] J. Wang, H. Wu, D. Gao, S. Miao, G. Wang, X. Bao *Nano Energy*. **2015**, 13, 387-396.
[64] Y. Liang, Y. Li, H. Wang, J. Zhou, J. Wang, T. Regier, H. Dai *Nat Mater*. **2011**, 10, 780-786.
[65] T. Y. Ma, J. Ran, S. Dai, M. Jaroniec, S. Z. Qiao *Angewandte Chemie International Edition*. **2015**, 54, 4646-4650.
[66] B. Aghabarari, M. V. Martinez-Huerta, M. Ghiaci, J. L. G. Fierro, M. A. Pena *RSC Advances*. **2013**, 3, 5378-5381.
[67] D. F. van der Vliet, C. Wang, D. Tripkovic, D. Strmcnik, X. F. Zhang, M. K. Debe, R. T. Atanasoski, N. M. Markovic, V. R. Stamenkovic *Nat Mater*. **2012**, 11, 1051-1058.

[68] I. Adebayo Akinbulu, T. Nyokong *New Journal of Chemistry*. **2010**, 34, 2875-2886.
[69] B. Agboola, K. I. Ozoemena, T. Nyokong *Electrochimica Acta*. **2006**, 51, 4379-4387.
[70] N. Ramaswamy, U. Tylus, Q. Jia, S. Mukerjee *Journal of the American Chemical Society*. **2013**, 135, 15443-15449.
[71] M.-S. Liao, S. Scheiner *The Journal of Chemical Physics*. **2002**, 117, 205-219.

Figures and Tables

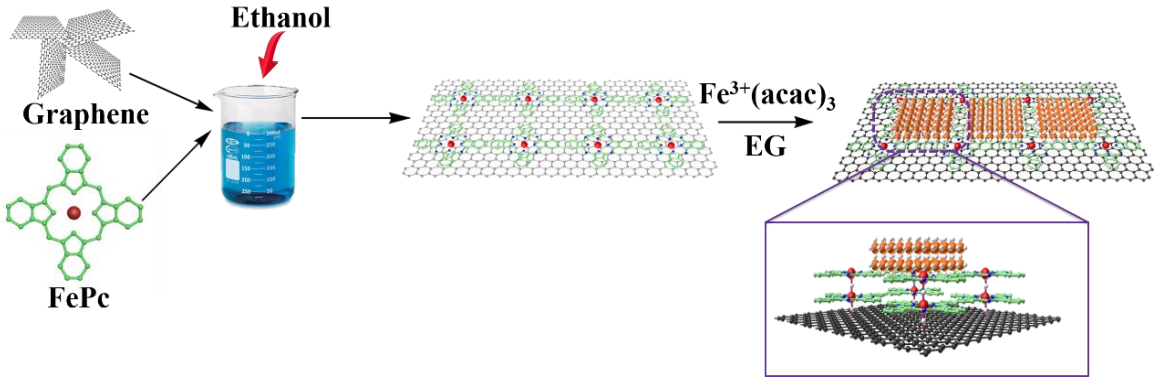

Figure 1. Procedure to synthesize FeO_x NCs supported on FePc functionalized graphene.

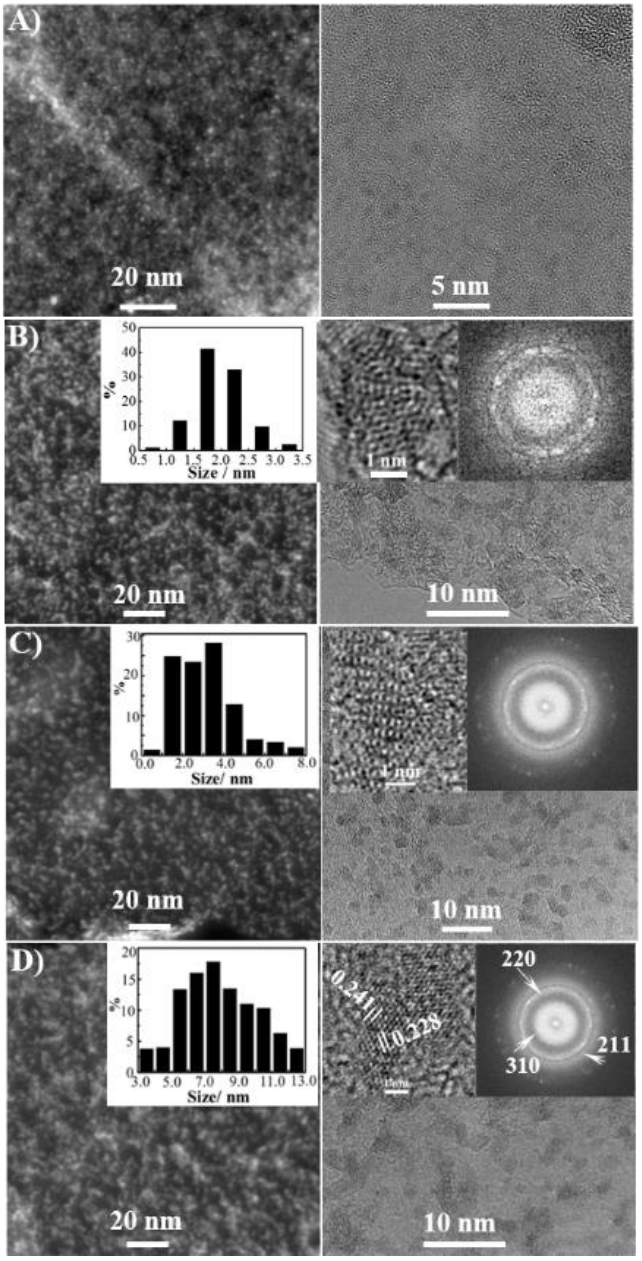

Figure 2. STEM (left), HRTEM (middle) micrographs and size histograms for A) FePc-G; B) FeO_x/FePc-10, C) FeO_x-FePc-20 and D) FeO_x/FePc-40.

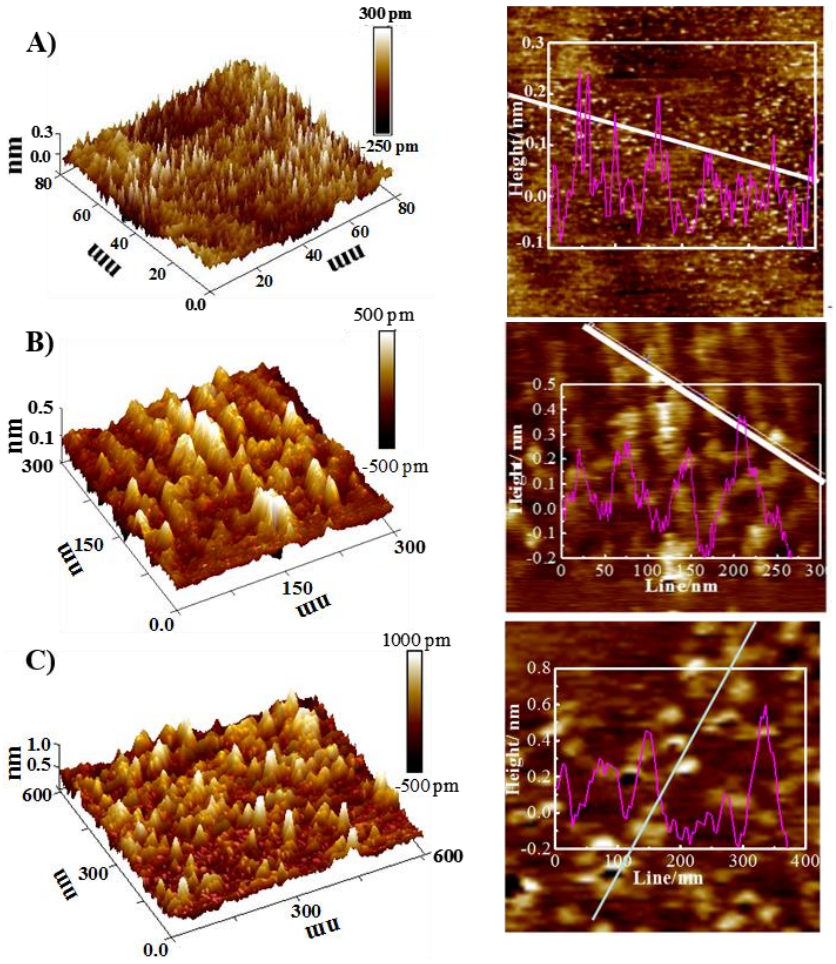

Figure 3. AFM micrographs and line scan analysis for A) FePc-G, B) FeO_x/FePc-10, and C) FeO_x/FePc-40.

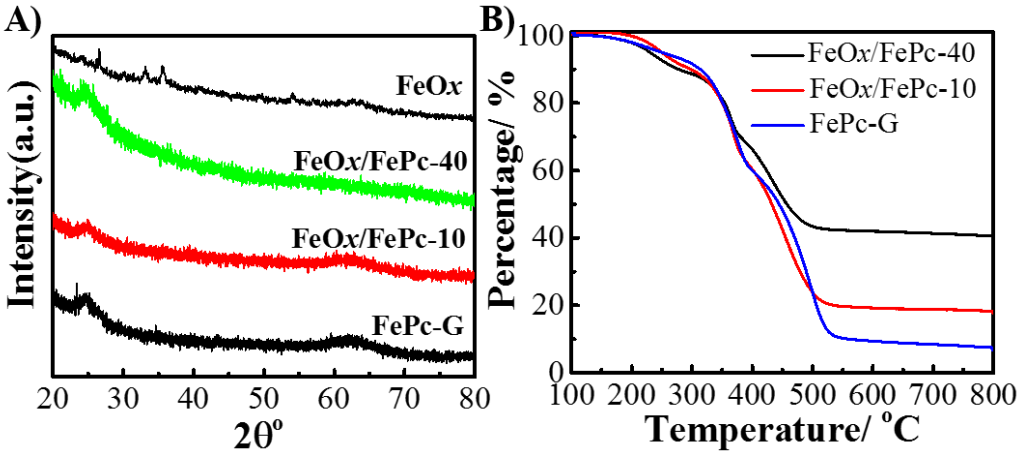

Figure 4. A) XRD patterns and B) TGA curves of FeO_x, FePc-G, FeO_x/FePc-10 and FeO_x/FePc-40.

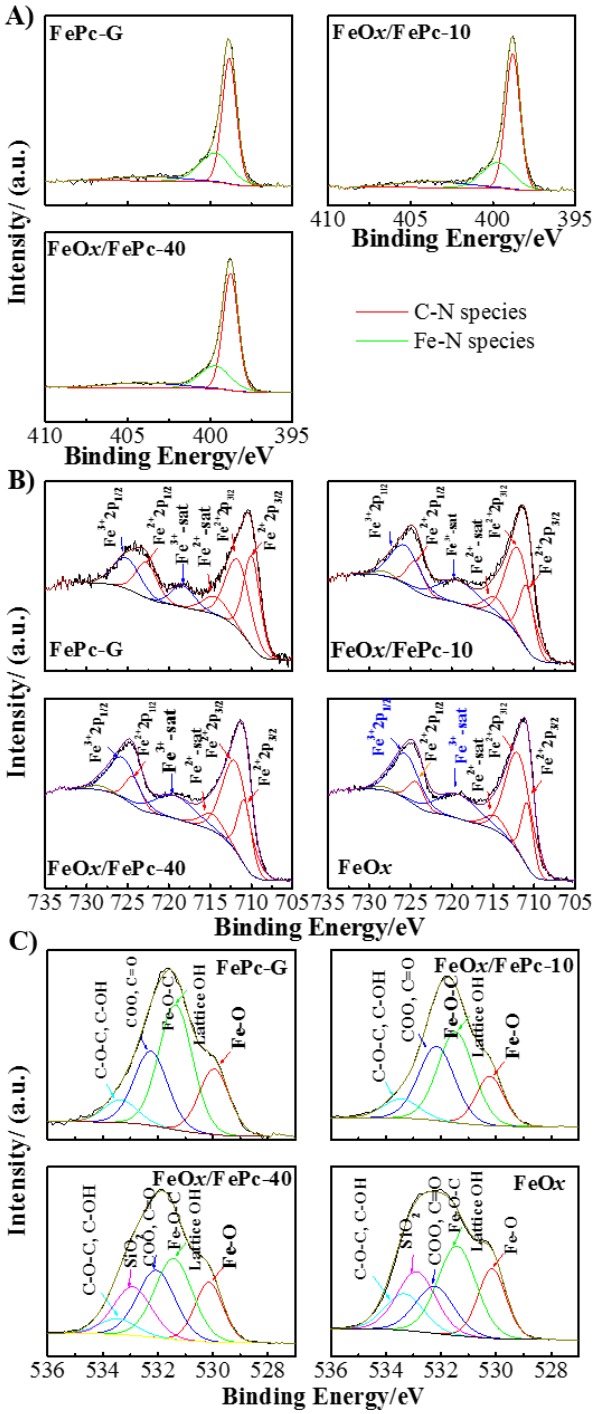

Figure 5. Deconvolution of high resolution XPS patterns of A) N 1s, B) Fe 2p, and C) O 1s for FePc-G, FeO_x/FePc-10, FeO_x/FePc-40, and FeO_x. Note: the SiO_2 contribution observed in the O 1s spectra arises due to the silicon substrate used.

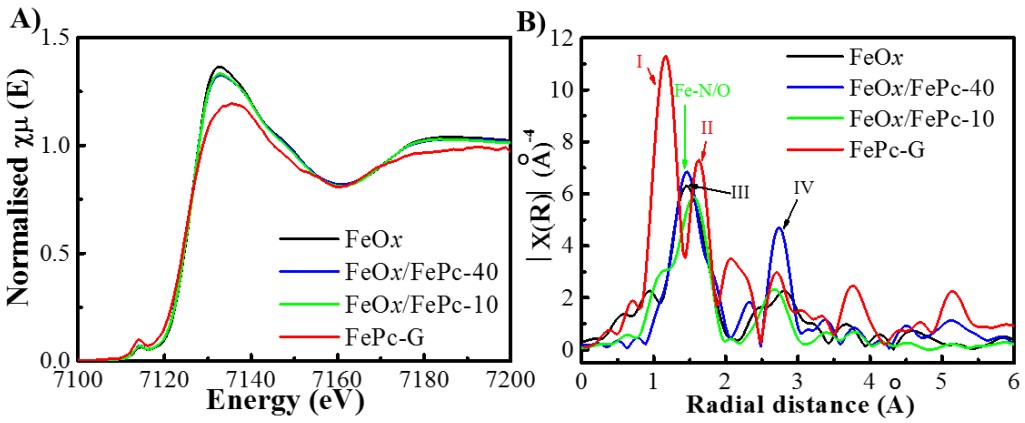

Figure 6. A) XANES spectra of FePc-G, FeO_x/FePc and FeO_x, B) The Fourier Transform (FT) at Fe K-edge of EXAFS data for FePc-G, FeO_x/FePc-10, FeO_x/FePc-40 and FeO_x.

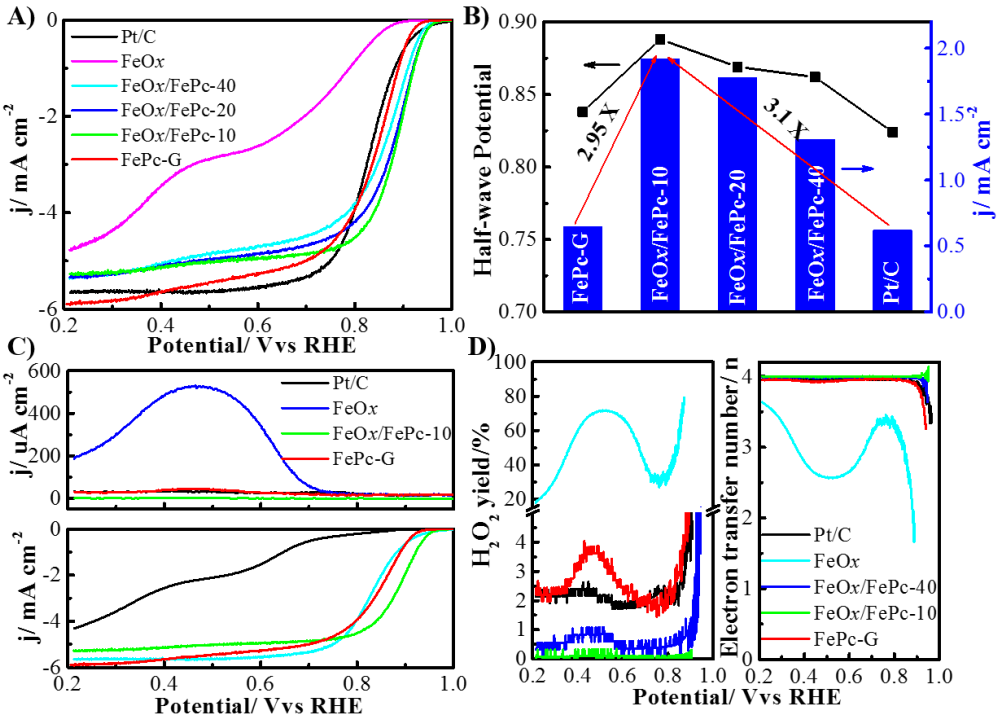

Figure 7. A) LSV curves of FePc-G, FeO_x/FePc-10, FeO_x/FePc-20, FeO_x/FePc-40, FeO_x and Pt/C, B) plots of half-wave potential and current density at 0.9 V; C) Rotating ring disk electrode shows the current density from the H_2O_2 produced during the ORR process, D) H_2O_2 yield and electron transfer number during the ORR process. The data were obtained in O_2-saturated 0.1 M KOH at scan rate of 10 mV s^{-1} and rotating rate of 1600 rpm with catalyst loading of 0.1 mg cm^{-2}.

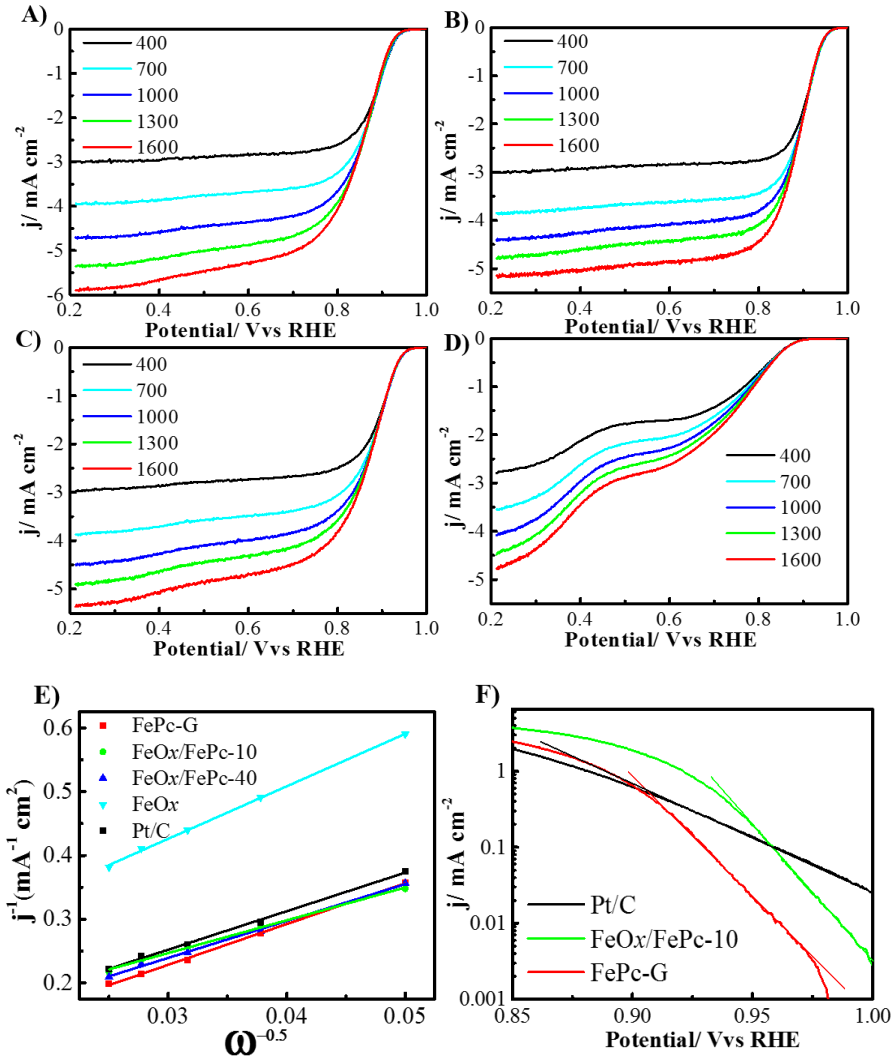

Figure 8. LSV curves of A) FePc-G, B) FeO_x/FePc-10, C) FeO_x/FePc-40 and D) FeO_x at different rotating rates, E) K-L curves obtained at 0.8 V, F) Tafel slopes of FePc-G, FeO_x/FePc-10 and Pt/C. The data were obtained in O_2-saturated 0.1 M KOH at scan rate of 10 mV s^{-1} and rotating rate of 1600 rpm with catalyst loading of 0.1 mg cm^{-2}.

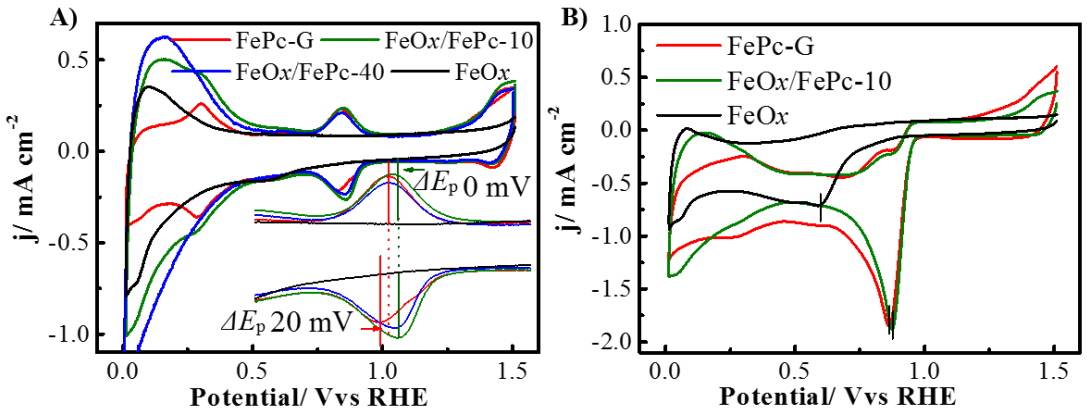

Figure 9. CV curves of FePc-G, FeO_x/FePc-10, FeO_x/FePc-40 and FeO_x in A) N_2-saturated, B) O_2-saturated 0.1 M KOH solutions with a scan rate of 0.05 V s^{-1}.

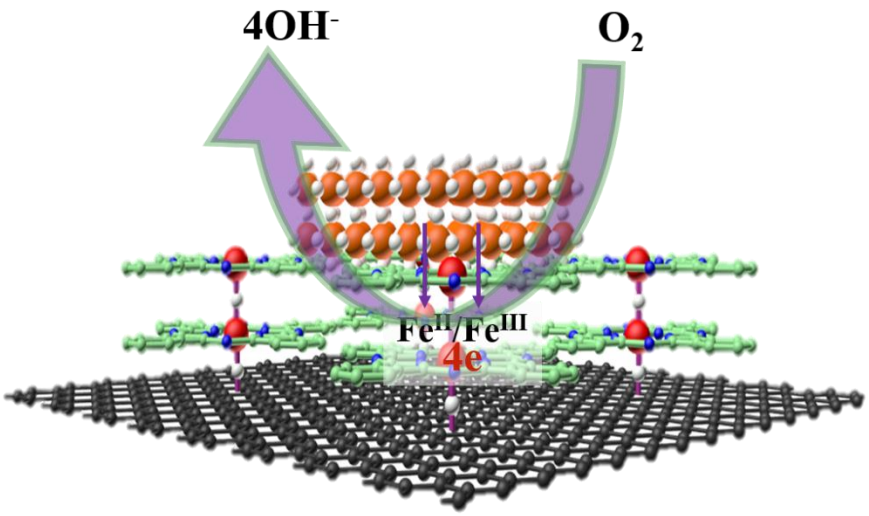

Figure 10. Scheme for ORR on FeO_x/FePc supported on graphene.

Table 1. Relative atomic concentration of the bonding species and binding energy of N 1s and Fe $2p_{2/3}$ based on XPS results.

Samples	Relative atomic concentration (%)				XPS	
	Fe-O	Fe-O-C, lattice OH^-	COO, C=O	C-O-C, C-OH	N 1s	Fe $2p_{2/3}$
Binding energy, eV	529.9	531.3	532.2	533.3	-	-
FePc-G	21.1	44.5	26.3	8.1	398.7	710.4
FeO_x/FePc-10	17.3	40.7	33.4	8.5	398.9	711.2
FeO_x/FePc-40	25.1	35.4	31.7	7.8	398.8	711.3
FeO_x	22.7	40.1	20.9	16.3	-	711.4

Table 2. ORR activities of typical NPMCs reported in literature.

Materials	Test condition		ORR		References
	Electrolyte (KOH)	Loading (mg cm^{-2})	E_{onset}	$E_{half\text{-}wave}$	
N-doped Fe/Fe_3C@graphitic layer/CNT	0.1 M	0.1	0.965	0.715	[57]
Fe(DFTPP)-CNTs	0.1 M	1.0	0.99	0.880	[58]
FePc/rGO	0.1 M	0.53	0.940	0.855	[33]
FePc–Py–CNTs	0.1 M	0.32	0.985	0.915	[60]
N-doped graphene/SWCNT	0.1 M	0.19625	0.880	0.68	[62]
Co/N-C	0.1 M	~0.25	0.834	0.75	[61]
Fe@N-carbon nanoshell	0.1 M	0.32	0.960	0.830	[63]
Co_3O_4/N-graphene	0.1 M	0.24	0.880	0.830	[64]
P-g-C_3N_4 carbon-fiber paper	0.1 M	-	0.90	0.63	[65]
N, P-graphene/carbon nanosheets	0.1 M	0.14	0.98	0.87	[59]
Atomically Dispersed Fe-N-C	0.1 M	0.6	0.95	0.85	[21]
Fe-N-CNT/PC	0.1 M	0.8	0.96	0.88	[22]
FePc-G	0.1 M	0.10	0.960	0.838	This work
FeO_x/FePc-10			0.990	0.888	This work
FeO_x/FePc-40			0.960	0.862	This work
FeO_x/FePc-20			0.975	0.869	This work
Pt/C			1.010	0.822	This work

* E_{onset} and $E_{half\text{-}wave}$ is obtained based on the linear scan voltammetry results from literature.